6-30-2015

Gravity Wave Propagation Through a Vertically and Horizontally Inhomogeneous Background Wind

C. J. Heale
Embry-Riddle Aeronautical University, HEALEC@erau.edu

J. B. Snively
Embry-Riddle Aeronautical University, snivelyj@erau.edu

AGU PUBLICATIONS

JGR

Journal of Geophysical Research: Atmospheres

RESEARCH ARTICLE
10.1002/2015JD023505

Key Points:
- Time-dependent medium-scale waves reduce reflection and critical-level effects
- Inhomogeneous background winds can vary the wavelengths of a small-scale wave
- GW parameterization schemes need to consider background time dependence

Correspondence to:
C. J. Heale,
healec@my.erau.edu

Citation:
Heale, C. J., and J. B. Snively (2015), Gravity wave propagation through a vertically and horizontally inhomogeneous background wind, *J. Geophys. Res. Atmos.*, *120*, 5931–5950, doi:10.1002/2015JD023505.

Received 13 APR 2015
Accepted 1 JUN 2015
Accepted article online 3 JUN 2015
Published online 30 JUN 2015

Gravity wave propagation through a vertically and horizontally inhomogeneous background wind

C. J. Heale[1] and J. B. Snively[1]

[1] Department of Physical Sciences, Embry–Riddle Aeronautical University, Daytona Beach, Florida, USA

Abstract A combination of ray theory and 2-D time-dependent simulations is used to investigate the linear effects of a time-dependent, vertically, and horizontally inhomogeneous background horizontal wind field on the propagation, refraction, and reflection of small-scale gravity wave packets. Interactions between propagating waves of different scales are likely to be numerous and important. We find that a static medium-scale wave wind field of sufficient amplitude can channel and/or critical-level filter a small-scale wave or cause significant reflection, depending upon both waves' parameters. However, the inclusion of a time-dependent phase progression of the medium-scale wave can reduce energy loss through critical-level filtering by up to ~70% and can also reduce reflection by up to ~60% for the cases simulated. We also find that the relative direction of propagation between the small-scale and medium-scale wave can significantly affect small-scale wave filtering. When the phases are progressing in the same horizontal direction, the small-scale wave is far more likely to become trapped and ultimately critical-level filtered than if the phases are propagating in opposite horizontal directions unless reflection occurs first. Considerations of time-dependent winds associated with medium-scale-propagating waves and their directionality are important for assessing the propagation and dispersion of small-scale waves over large horizontal distances.

1. Introduction

Small-scale gravity waves are known to play a significant role in the dynamics of the middle atmosphere [*Fritts and Vincent*, 1987; *Oliver et al.*, 1997; *Fritts and Alexander*, 2003; *Djuth et al.*, 2004]. Through mechanisms such as wave breaking, dissipation, and critical-layer filtering, gravity waves are able to deposit their energy and momentum into the background flow [*Pitteway and Hines*, 1963; *Lindzen*, 1981; *Holton*, 1982, 1983; *Fritts*, 1984; *Fritts et al.*, 1996, 2006; *Vadas and Fritts*, 2006; *Vadas*, 2007; *Yiğit et al.*, 2008, 2009; *Vadas and Liu*, 2009; *Fritts and Lund*, 2011; *Waterscheid and Hickey*, 2011; *Heale et al.*, 2014b]. They provide one of the key methods of energy and momentum transport from the troposphere to the mesosphere and lower thermosphere (MLT) [*Hung and Kuo*, 1978; *Lindzen*, 1981; *Holton*, 1982; *Vincent and Reid*, 1983; *Fritts and Dunkerton*, 1985; *Kelley*, 1997; *Hocke and Tsuda*, 2001].

Gravity waves are subject to refraction as they propagate, due to the varying background atmospheric temperature structure and winds. While the temperature structure varies the local buoyancy frequency, the background wind acts to Doppler shift the intrinsic frequency of the waves. Wave propagation through a vertically sheared horizontal wind has been extensively studied both theoretically and experimentally [e.g., *Bretherton*, 1966; *Booker and Bretherton*, 1967; *Thorpe*, 1981; *Hartman*, 1975; *Dunkerton and Fritts*, 1984] and numerically [e.g., *Zhang and Yi*, 2002; *Vadas and Fritts*, 2006; *Yu et al.*, 2009; *Liu et al.*, 2013; *Heale et al.*, 2014b]. If the intrinsic frequency of a wave is shifted to the local buoyancy frequency then, under the Boussinesq approximation, the vertical wave number goes to zero and the wave encounters a turning point, beyond which the wave takes on an evanescent exponentially decaying form [*Lighthill*, 1978; *Blumen*, 1985; *Dunkerton*, 1981; *Robinson*, 1997; *Sutherland*, 1999, 2000]. If two turning point levels are present at two different altitudes then waves can be ducted, meaning that they are trapped between the two altitudes and travel predominantly horizontally rather than vertically [*Chimonas and Hines*, 1986; *Wang and Tuan*, 1988; *Fritts and Yuan*, 1989; *Isler et al.*, 1997; *Taylor et al.*, 1995; *Walterscheid et al.*, 1999; *Snively et al.*, 2007; *Yu and Hickey*, 2007; *Snively and Pasko*, 2008; *Heale et al.*, 2014b]. Alternatively, if the wind Doppler shifts the wave so that its intrinsic frequency approaches zero, then the vertical wavelength approaches zero also, and the wave undergoes

critical-level filtering. This effect, along with source distributions, has been noted as a primary explanation for observed wave directional anisotropies [*Hecht et al.*, 2001; *Walterscheid et al.*, 2001].

While many parameterization schemes consider small-scale gravity waves as exclusively vertically propagating, the fact remains that waves can be ducted and can propagate large horizontal distances, depositing their energy and momentum in the MLT far from their source region [*Yu and Hickey*, 2007; *Suzuki et al.*, 2013a, 2013b; *Heale et al.*, 2014a].

Waves at larger scales (such as planetary waves, tides, medium-scale, and inertial-scale gravity waves) can appear as horizontally inhomogeneous and time-dependent background winds to smaller-scale waves. Airglow image 'Keograms' show that there is a large spectrum of wave scales interacting in the mesosphere [e.g., *Taylor et al.*, 2009].

The propagation of small-scale gravity waves in a time-dependent inertial gravity wave background has been studied using ray tracing techniques and numerical models in the $z-t$ domain [e.g., *Broutman and Young*, 1986; *Eckermann*, 1997; *Walterscheid*, 2000; *Sartelet*, 2003; *Vanderhoff et al.*, 2008; *Senf and Achatz*, 2011]. Three limits of importance were identified: $C_g << C_{bg}$, $C_g = C_{bg}$, and $C_g >> C_{bg}$, where C_g is the vertical group velocity of the small-scale wave and C_{bg} is the vertical phase speed of the background wave. When $C_g >> C_{bg}$, the background wave appears almost static to the small-scale wave and critical-level interactions are frequent, while trapping is frequent when $C_g = C_{bg}$. *Broutman and Young* [1986] also suggest that large permanent decreases in the small-scale wave number can occur when $C_g << C_{bg}$. All of the studies are in agreement that the inclusion of the time dependence of the background tends to inhibit the presence of critical levels and increase transmission of waves through a background wave.

While the effect of vertically sheared winds are well known and time dependence has been studied, the effect of horizontally varying winds are less well known. *Huang et al.* [2008] performed simulations of a gravity wave propagating through a meridionally sheared zonal wind and demonstrated the horizontal reflection of a gravity wave packet. They noted that while the zonal perturbation showed an evanescent configuration beyond the reflection point, the meridional perturbation velocity did not. If the sheared wind was not strong beyond the reflection point, then the wave packet could be partially transmitted. Theoretical work into the effects of horizontal shears on wave propagation has been performed by *Basovich and Tsimring* [1984], *Badulin et al.* [1985], *Badulin and Shriria* [1993], and *Bakas and Farrell* [2008], predominantly using WKB theory [*Bretherton*, 1966; *Einaudi and Hines*, 1971; *Olbers*, 1981; *Badulin and Shriria*, 1993], and primarily considering the context of internal waves in the ocean. They predict effects such as wave "blocking," in which the wave's horizontal group velocity becomes zero against an opposing background wind. In addition, wave trapping is predicted for parallel flows where the intrinsic frequency equals the buoyancy frequency and the horizontal wave number and amplitude grow indefinitely in the inviscid, linear regime.

In this paper, we investigate the propagation of two small-scale wave packets of small amplitude through three different background wind conditions: (1) a purely vertically or horizontally varying horizontal wind field, (2) a static and time-dependent background medium-scale wave whose phase progresses in the direction of the small-scale wave, and (3) the same background wave but with phase progressing against the small-scale wave. A combination of ray tracing and 2-D compressible numerical simulations are performed to investigate the effect of a time-dependent background wind in reducing extreme effects such as critical-level filtering and also reflection. The paper is arranged as follows: Section 2 describes the numerical model, simulation parameters, and ray theory. Section 3 describes the results from the purely vertically or horizontally varying background wind. Section 4 describes the results from the medium-scale wave backgrounds; finally, section 5 provides discussion and conclusions.

2. Numerical Model and Domain

2.1. Governing Equations and Background Atmosphere

The numerical model utilizes a modified set of the Clawpack libraries [*LeVeque and Berger*, 2004], in the form described by *Snively and Pasko* [2008] and *Snively* [2013]. The equations solved are the nonlinear, fully compressible, Euler equations with the inclusion of two separately solved equations describing molecular viscosity and thermal conductivity.

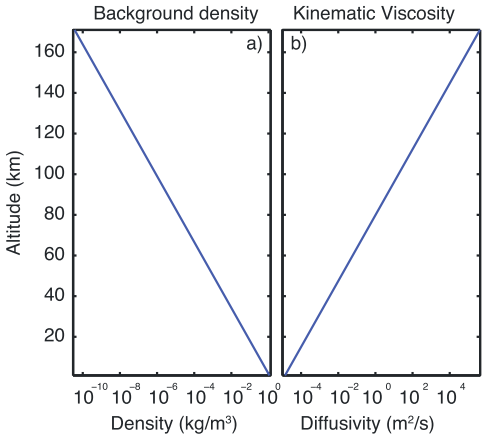

Figure 1. (a) The background density profile for all simulations. (b) The kinematic viscosity profile for all simulations (note: $Pr = 1$).

The method for solving the Euler equations involves solving a Riemann problem at each cell boundary by decomposing the flux differences between cells into characteristic eigenvalues and eigenvectors of the Roe-averaged Jacobian matrices of the system of equations [*Roe*, 1981; *Bale et al.*, 2002; *LeVeque and Berger*, 2004]. These sets of eigenvectors and eigenvalues represent the "waves" traveling from the cell boundaries (with the eigenvalues representing the wave speeds). The waves can be summed over the left and right going components to form a finite volume solution to the Euler equations at the next time step.

In the vertical direction, flux differences between grid cells arise from the vertical pressure gradient, which is subsequently balanced by the gravitational term. However, in the horizontal the flux differences between cells are zero naturally unless there is a horizontally inhomogeneous background. If we introduce a background horizontally inhomogeneous wind to the simulation, then the background wind will evolve in time as governed by the system of equations. In order to analyze small-scale gravity wave propagation through a nonevolving horizontally inhomogeneous wind, we need to introduce an artificial horizontal pressure gradient to hold the background wind field in place. For the system

$$\frac{\partial}{\partial t}\begin{bmatrix}\rho\\ \rho u\\ \rho w\\ E\end{bmatrix}+\frac{\partial}{\partial x}\begin{bmatrix}\rho u\\ \rho u^2+p\\ \rho uw\\ u(E+p)\end{bmatrix}+\frac{\partial}{\partial z}\begin{bmatrix}\rho w\\ \rho uw\\ \rho w^2+p\\ w(E+p)\end{bmatrix}=\psi+\psi_g+\psi_d\,, \tag{1}$$

where u and w denote velocities in the horizontal and vertical directions, and ψ_g and ψ_d represent gravity and dissipation, respectively. The second bracket represents the horizontal fluxes, and the first, second, and fourth rows will have nonzero values in the presence of a horizontally varying background wind $\frac{du}{dx}$ (the third is zero since w is zero). We introduce an effective source term (ψ) which is equal and opposite to these flux differences at $t = 0$ and applies throughout the duration of the simulation.

$$\psi=\frac{\partial}{\partial x}\begin{bmatrix}\rho u\\ \rho u^2+p\\ \rho uw\\ u(E+p)\end{bmatrix}_{t=0}\,, \tag{2}$$

where ρ and p are the density and pressure, respectively, T is the temperature, g is the acceleration due to gravity, γ is the ratio of specific heats, and E is the energy. Note that no sponge layer (Rayleigh friction) is used, and for our isothermal atmosphere γ was specified to be 1.4 at all altitudes. The background atmosphere is specified with a temperature of $T = 239$ K, with the pressure and density at ground given by $P_0 = 82311.6$ Pa, and $\rho_0 = 1.2$ kg m^{-3}, respectively. The scale height $H = RT/g = 7$ km and $R = 287$ J kg^{-1}K^{-1}. The density and viscosity profiles are shown in Figures 1a and 1b, respectively. The parameters ν and κ are the kinematic molecular viscosity and thermal conductivity, respectively, with the kinematic molecular viscosity (m^2/s) taken from *Banks and Kockarts* [1973]

$$\nu = 3.5\times10^{-7}T(z)^{0.69}/\rho(z)\,. \tag{3}$$

The thermal conductivity is related to the molecular viscosity via the Prandtl number $Pr = \nu/\kappa$, which is set to 1 for these idealized simulations.

2.2. Ray Trace Equations

The ray trace equations are adapted from *Lighthill* [1978] and describe the evolution of the wave numbers, frequency, and position of a wave packet through a varying background atmosphere (in the absence of viscosity):

$$\frac{d\vec{x}}{dt} = \vec{c}_g \tag{4}$$

$$\frac{dm}{dt} = -k\frac{\partial u}{\partial z} \tag{5}$$

$$\frac{dk}{dt} = -k\frac{\partial u}{\partial x} \tag{6}$$

$$\frac{d\omega}{dt} = k\frac{\partial u}{\partial t}, \tag{7}$$

with the group velocities specified under Boussinesq conditions by

$$C_{gx} = u_0 + \frac{m^2}{N^2}(c - u_0)^3 \tag{8}$$

$$C_{gz} = -\frac{km}{N^2}(c - u_0)^3, \tag{9}$$

where $\vec{x}$ is the position vector (x,z), k is the horizontal wave number, m is the vertical wave number, ω is the angular frequency, c is the phase speed, and N is the buoyancy frequency.

In this paper, we are only interested in the raypaths and not the amplitudes. This simplifies analysis considerably, although we do not account for realistic behavior at caustics. A group of rays are traced from the same initial altitude with the same initial wave numbers and frequency. However, the initial x locations of the rays lie along the horizontal width of the small-scale gravity wave packet in 10 km intervals.

2.3. Numerical Domain, Background Wind, and Small-Scale Wave Source

The numerical domain is set to be 600 km horizontally by 170 km vertically with a 0.5 km resolution in both. The lower boundary ($z = 0$) is set as closed (Dirichlet condition), the upper boundary ($z = 170$ km) is open (Neumann condition), and the two side boundaries ($x = 0, 600$ km) are also open. Simulations were run for 7500 s with frames output every 15 s, the time step used was 0.8 of a second. The background wind field is specified via the following equation:

$$\begin{aligned} U_0(x,z,t) = A_0 \exp\left[-\frac{(z-z_0)^2}{2\sigma_{0z}^2} - \frac{(x-x_0)^2}{2\sigma_{0x}^2}\right] \times \\ \exp\left(\frac{z-z_0}{2H}\right)\cos[K(x-x_0) + M(z-z_0) - \omega t]. \end{aligned} \tag{10}$$

In this paper we utilize three different background wind fields: (BG1) A background horizontal wind which varies in either the (a) vertical or (b) horizontal direction only, which is specified by a Gaussian in x or z and is for validation purposes only; (BG2) A medium-scale background "wave" ($\lambda_x = 228$ km, $\lambda_z = 20$ km, Period = 1 h), specified by the horizontal wind field, and traveling "rightward" (positive K); and (BG3) The same as BG2 but traveling "leftward" ($-K$). The exact parameters will be specified in the relevant sections. Examples of the background winds are shown in Figure 2.

The small-scale gravity wave packet is specified via an initial horizontal perturbation velocity given by

$$\begin{aligned} u'(x,z,t=0) = A_1 \exp\left[-\frac{(z-z_1)^2}{2\sigma_z^2} - \frac{(x-x_1)^2}{2\sigma_x^2}\right] \times \\ \exp\left(\frac{z-z_1}{2H}\right)\cos[k(x-x_1) + m(z-z_1)]. \end{aligned} \tag{11}$$

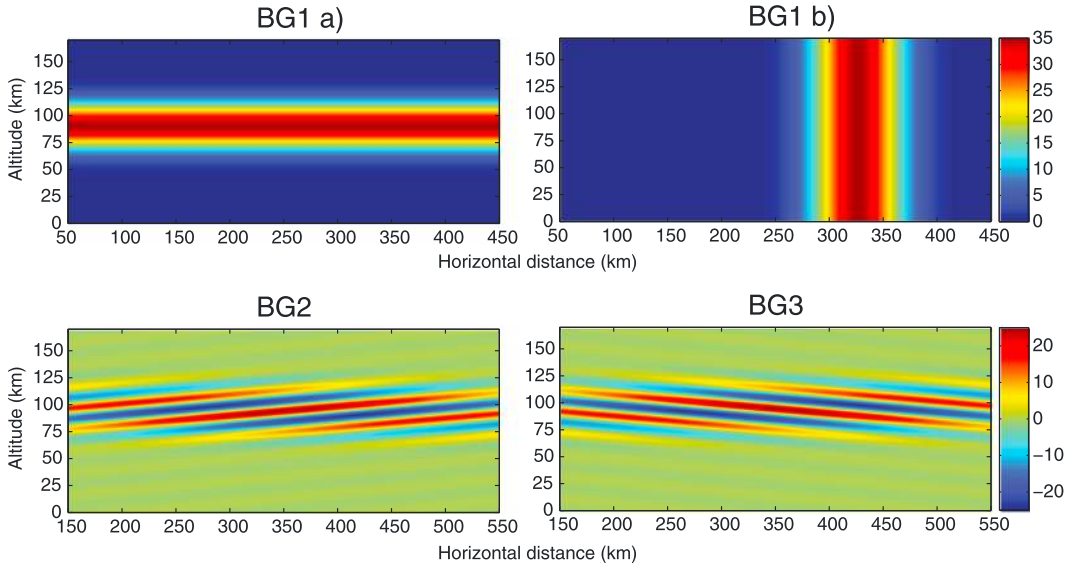

Figure 2. The background horizontal wind conditions used in this paper. Note that for BG1(a) and BG1(b), we also propagate the small-scale wave through these winds with a peak of −35 m/s in each case.

The other perturbation quantities are related to this via the polarization relations [e.g., *Fritts and Alexander*, 2003]. Two small-scale gravity wave packets are used in this paper: packet "SSGW1" which is more susceptible to critical-level interactions than it is to reflections ($\lambda_x = 20$ km, $\lambda_z = 10$ km, Period = 11.76 min) and packet "SSGW2" which is more susceptible to reflection than it is to critical-level interactions ($\lambda_x = 18$ km, $\lambda_z = 18$ km, Period = 7.4 min). The "susceptibility" to these conditions is assessed by the relative magnitude of wind needed to induce a critical or reflection level. In each case, $A_1 = 1 \times 10^{-3}$ m/s, $z_1 = 35$ km, $\sigma_z = \lambda_z$, $x_1 = 250$ km, and $\sigma_x = 30$ km. Please note that all figures display the density-scaled horizontal winds, i.e., the raw velocity multiplied by $(\rho(z)/\rho(z_1))^{1/2}$.

3. Purely Vertically and Horizontally Inhomogeneous Background Wind

For validation purposes, we begin by specifying background winds which vary in the vertical or horizontal directions alone. It is specified by a simple Gaussian in z or x of $\sigma_{0z} = 15$ km and $\sigma_{0x} = 30$ km half width, respectively, with a peak wind amplitude of $A_0 = \pm 35$ m/s at $z = 95$ km and $x = 325$ km, respectively. We allow SSGW1 to propagate through the vertically or horizontally varying background wind plotting the results at five different time steps in Figure 3 and overlay the ray trace paths. We compare the changes in wavelengths predicted by equations (6) and (5) with the wavelengths measured directly from the numerical simulation results along the raypaths using a wavelet transform of *Torrence and Compo* [1998] in Figure 4.

For the purely vertically varying horizontal background wind, the small-scale gravity wave is subject to either critical-level filtering, when the wave propagates with the wind, or reflection, when the wave opposes the mean wind. Both effects can be seen clearly in Figure 3. Critical-level filtering occurs when the ground relative phase speed of the small-scale wave is equal to the magnitude of the background wind and the vertical wavelength approaches zero while the horizontal wavelength remains constant (Figure 4). Reflection occurs when the intrinsic frequency of the wave approaches the local buoyancy frequency of the atmosphere. Here the vertical wavelength approaches infinity before the vertical wave number switches sign. For a packet, the wave energy is partially reflected and partially transmitted, with the relative amplitudes predominantly depending upon the depth of the evanescent layer that the wave encounters. As can be seen, one limitation with the ray trace path is that it predicts a total reflection of the wave and does not account for transmission.

In the case of a purely horizontally varying background wind, which is not time dependent, we assume that ω and m are now constant and only k varies with time. This means that the ray trace equations (5) and (7) are not needed. From equation (6) the horizontal wave number changes in response to the horizontal gradient

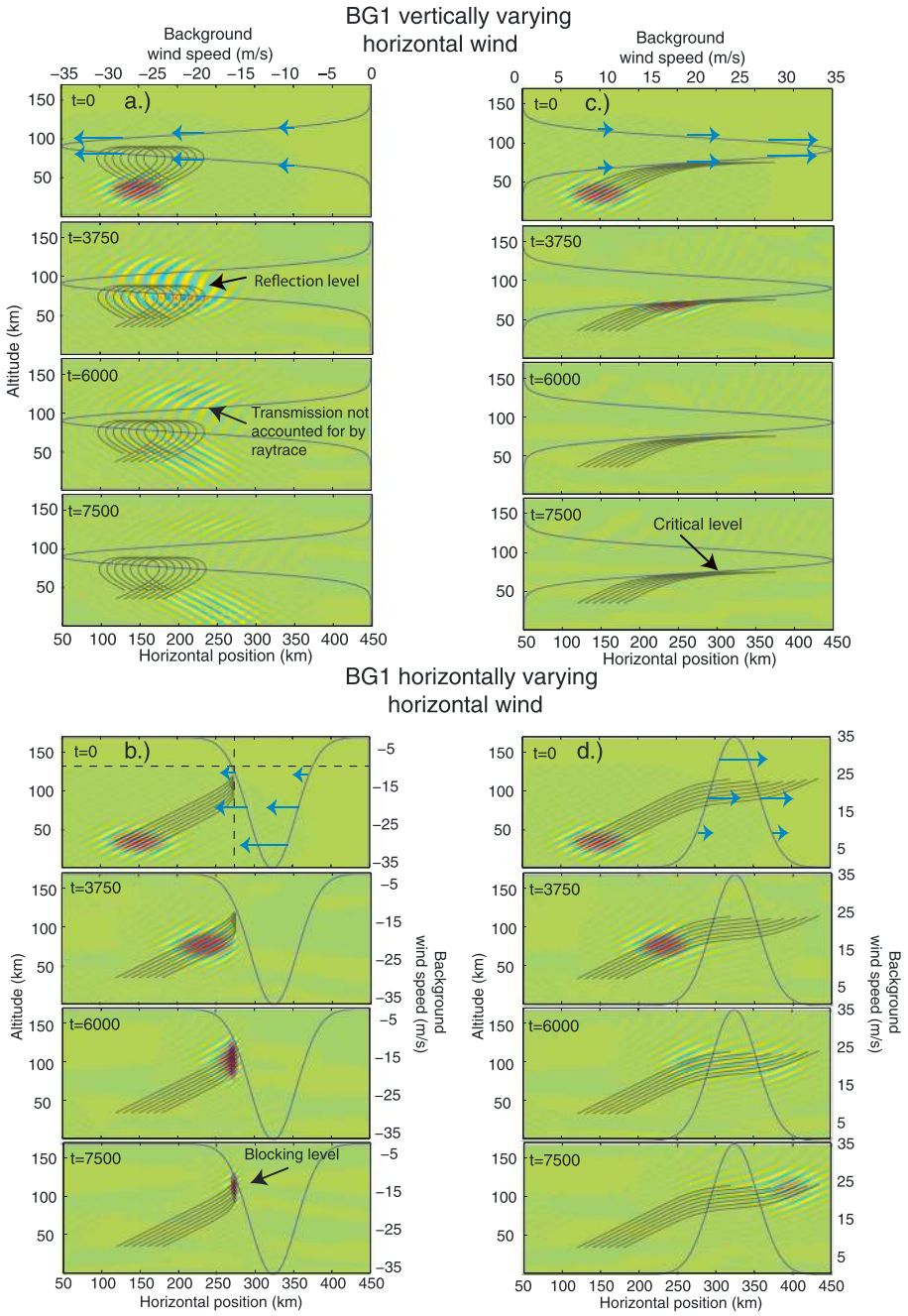

Figure 3. The propagation of SSGW1 through a (a,c) vertically varying and (b,d) horizontally varying horizontal wind at four different times. The black lines represent the ray trace paths and the blue Gaussian represents the background wind profile. Figures 3a and 3b represent the −35 m/s wind peak simulations and Figures 3c and 3d represent the +35 m/s wind peak simulations.

of the horizontal wind. If the gradient is positive, then the horizontal wave number will decrease with time, and if it is negative, then the horizontal wave number will increase in time.

Figure 3b shows the case where SSGW1 propagates against the background flow whose gradient is negative as the packet approaches. In this case, the opposition between the sign of the horizontal wave number and background wind causes the horizontal wavelength to decrease with the increasingly negative background wind (Figure 4). As time increases, the well-formed Gaussian packet is "compressed" from its right-hand edge

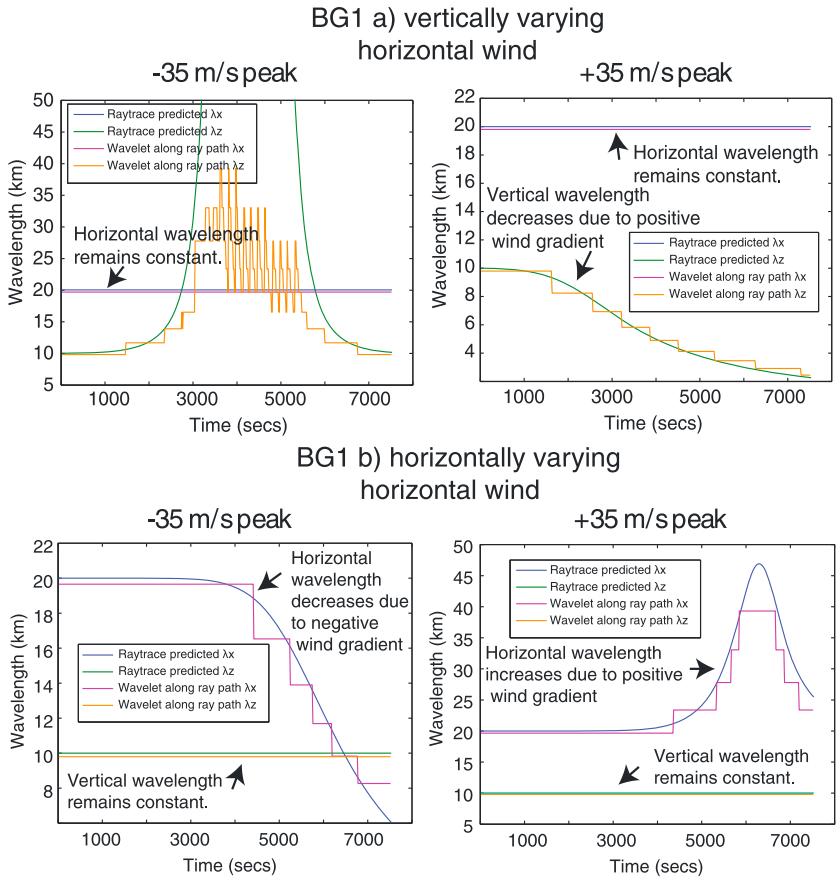

Figure 4. The changes in vertical and horizontal wavelengths predicted by the ray trace equations as compared with a wavelet analysis for BG1: (a) the vertically varying and (b) the horizontally varying horizontal winds cases. The left column represents the −35 m/s wind peak simulations and the right column represents the +35 m/s wind peak simulations.

as the horizontal wavelength shrinks and the wave is refracted to a more vertical trajectory. Eventually, the packet encounters what appears similar to a critical level for vertical shears [*Booker and Bretherton*, 1967], but in theory this cannot occur since the intrinsic frequency should always remain positive. This effect has been described as "blocking" in the context of surface ocean waves and is described for internal waves in section 2.2 of *Basovich and Tsimring* [1984]. They describe this as a position where the horizontal group velocity v_{gx} goes to zero and the packet ceases to propagate horizontally. At the same time the packet reflects and wave crests move against the flow, while the envelope moves with the flow. They also note that k increases as U decreases. The ray trace equations show that λ_z remains constant, while λ_x tends toward smaller values with time (and thus increasingly negative U) as predicted by *Basovich and Tsimring* [1984]. The wavelet-transform-derived wavelengths agree well with the ray trace predictions as do the raypaths with the numerical simulation.

The blocking level in Figure 3b occurs at $x = 274$ km, where the background wind has a value of −8.5 m/s. The prediction made by *Basovich and Tsimring* [1984] is that a blocking level would occur when the background wind has a magnitude of

$$u_0 = \frac{\left(N^{\frac{2}{3}} - \omega^{\frac{2}{3}}\right)^{\frac{3}{2}}}{m}, \tag{12}$$

which, for the values in our simulation, would yield a background wind speed of −8.57 m/s. Therefore, our model agrees well with the theory in this instance.

Figure 3d shows the case when SSGW1 is propagating with the background wind, with a positive gradient as the packet approaches. In this instance, the wave packet is accelerated (horizontal group velocity increases) through the increasingly positive wind and then slows down again when it has propagated beyond the background wind peak at $x = 325$ km, and the background wind gradient becomes negative. As a result, the packet becomes "stretched" in the horizontal direction as the wave is refracted to a more horizontal trajectory and begins to split into two packets at $t = 6000$ s. The horizontal wavelength in Figure 4 shows a shape similar to the Gaussian background wind, peaking at a value of ~47 km. The horizontal wavelength derived from the wavelet transforms agrees well with the ray trace equations but underestimates the peak, due to finite resolution.

4. Propagation Through a Medium-Scale Background Wave

In this section, the background horizontal wind is specified to take the form of a medium-scale background wave. In reality, a true background wave would consist of vertical wind, density, and temperature perturbations as well as a horizontal velocity perturbation; however, it has been suggested that the effects of such are small [*Eckermann*, 1997]. The temperature perturbations would change the background buoyancy frequency and can affect the propagation of the small-scale wave; however, this will be addressed in further studies. We also do not include the effect of the small-scale wave on the medium-scale wave; however, we keep the amplitude of the small-scale wave deliberately small so the interaction remains linear. The parameters of the two wave fields (BG2 and BG3) are as follows: $A_0 = 25$ m/s, $K = \pm 2\pi/228$ km, $M = 2\pi/20$ km, $\sigma_{0x} = 228$ km, $\sigma_{0z} = 15$ km, $x_0 = 350$ km, $z_0 = 95$ km, and $\omega = 2\pi/1$ h. The difference between the two is the direction of propagation relative to the small-scale gravity wave. BG2 propagates in the same direction as the small-scale wave, whereas BG3 and the small-scale wave have opposing horizontal propagation directions. Note that it is only the phase of the background wave which progresses, there is no associated group velocity (this will be performed in future studies).

We perform simulations to construct a comparison between small-scale wave propagation through the background wave when it is static and when the time-dependent phase progression is included. We propagate both SSGW1 and SSGW2 through these background wave fields to examine the effects of the omission and inclusion of phase progression of the background wave on critical levels and reflection. In each plot (Figures 5–8) we overlay the background wave wind field (faded) on top of the small-scale perturbation wind field; note, however, that this has no bearing on the relative magnitudes of the two; it is included only for illustration. In addition, the ray trace paths are overlaid on each initial plot for the time-independent backgrounds, with one ray highlighted in red. Measurements of the change in wave parameters (wavelength, period, and horizontal phase speed) and background wind field along the red raypath are displayed. While ray tracing is also performed for the time-dependent background cases, the paths are not overlaid of the figures. This is because the paths are time dependent; however, the plots shown are displayed at individual time steps. Therefore, the ray trace paths will not match the simulation path when considering a single frame at any given time. However, the change in parameters with time are displayed in Figures 5b, 5c, 5e, 5f, 6b, 6c, 6e, 6f, 7b, 7c, 7e, 7f, 8b, 8c, 8e, and 8f.

4.1. Propagation of SSGW1

Figure 5a shows the wave propagation at four different times for the static background wave wind field case (BG2). The small-scale wave is refracted by the phase fronts of the background wind and ultimately becomes channeled along lines of constant phase of the background wind, while being reduced in both horizontal and vertical scale. The ray trace paths match well with the 2-D simulation and show that the packet gets split into two sections, along two different phase fronts of the background wave; these then both undergo significant reduction in amplitude as they experience critical-level filtering. Figure 5b shows the changes in wavelength and period as measured along the red raypath in Figure 5a. Since the background wind is static, the period of the small-scale wave remains constant in time [*Lighthill*, 1978]. The vertical and horizontal wavelengths decrease and increase simultaneously (showing that the gradient of the background wind field in x and z are of the same sign at any given time) and, at late times, both approach zero as the wave experiences critical-level filtering and the small-scale wave becomes trapped along the phases fronts of the background wave. The trapping of the wave can also be seen in Figure 5c, the wind varies far more slowly along the raypath at late times as the small-scale wave becomes channeled along a constant phase front of the background wind, and the horizontal phase speed of the small-scale wave approaches the background wind value (the critical-level condition).

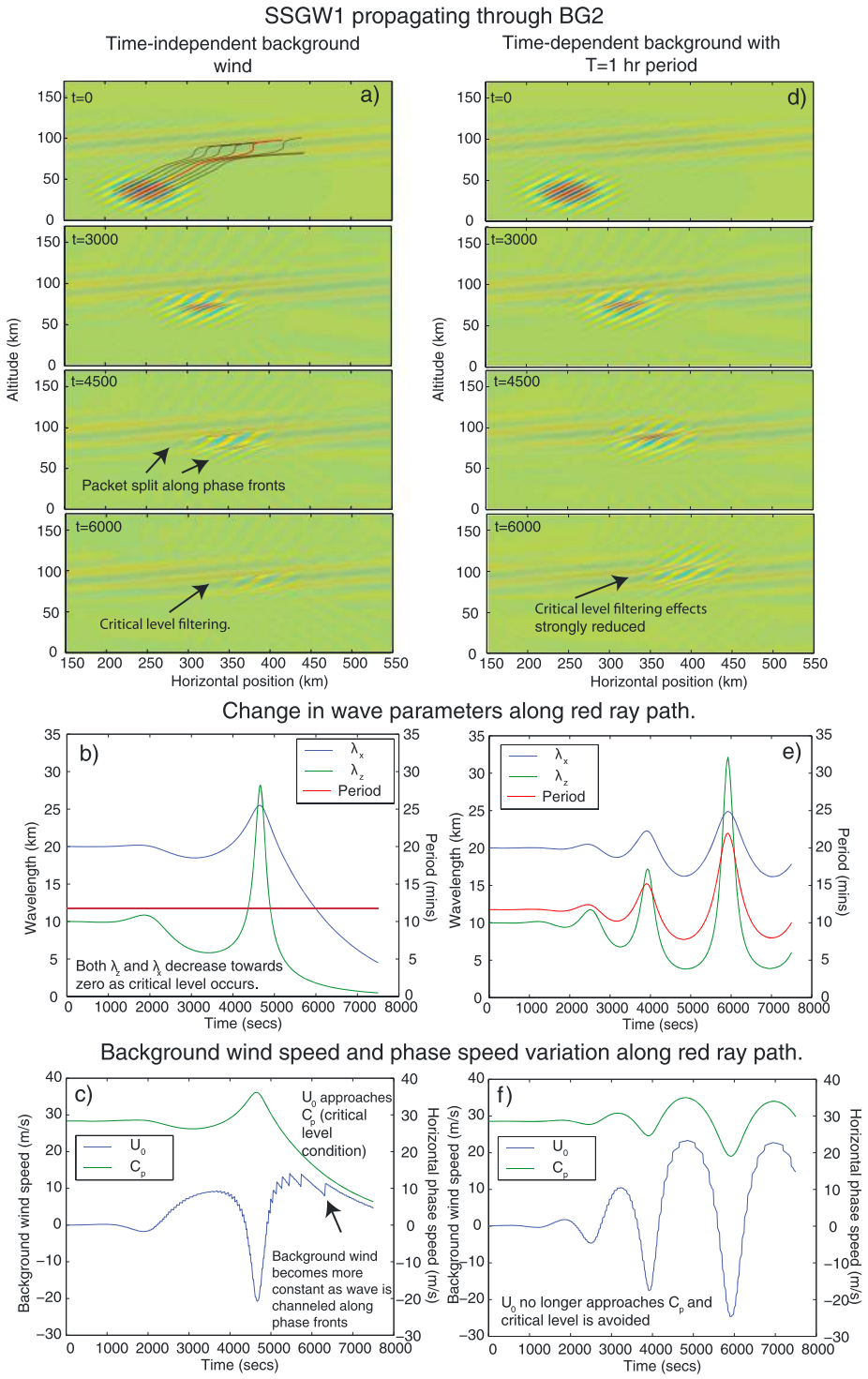

Figure 5. The propagation of SSGW1 through BG2 at four different times for (a) the time-independent background case and (d) adding a time-dependent phase progression of the background wave. The black lines represent the ray trace paths and the remaining figures show the changes in (b,e) wave parameters and (c,f) background wind and small-scale wave phase speed along the raypath.

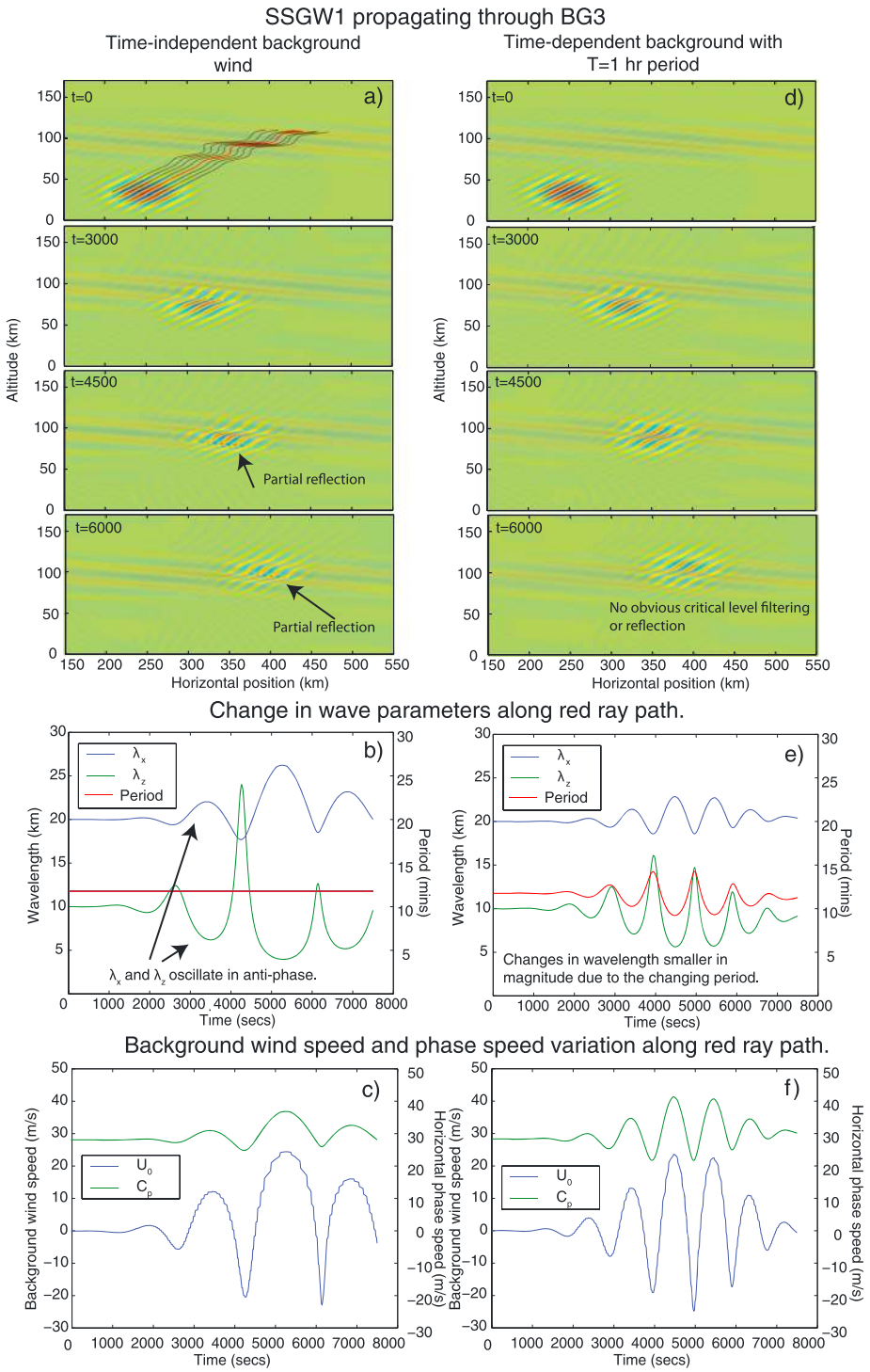

Figure 6. The propagation of SSGW1 through BG3 at four different times for (a) the time-independent background case and (d) adding a time-dependent phase progression of the background wave. The black lines represent the ray trace paths, and the remaining figures show the changes in (b,e) wave parameters and (c,f) background wind and small-scale wave phase speed along the raypath.

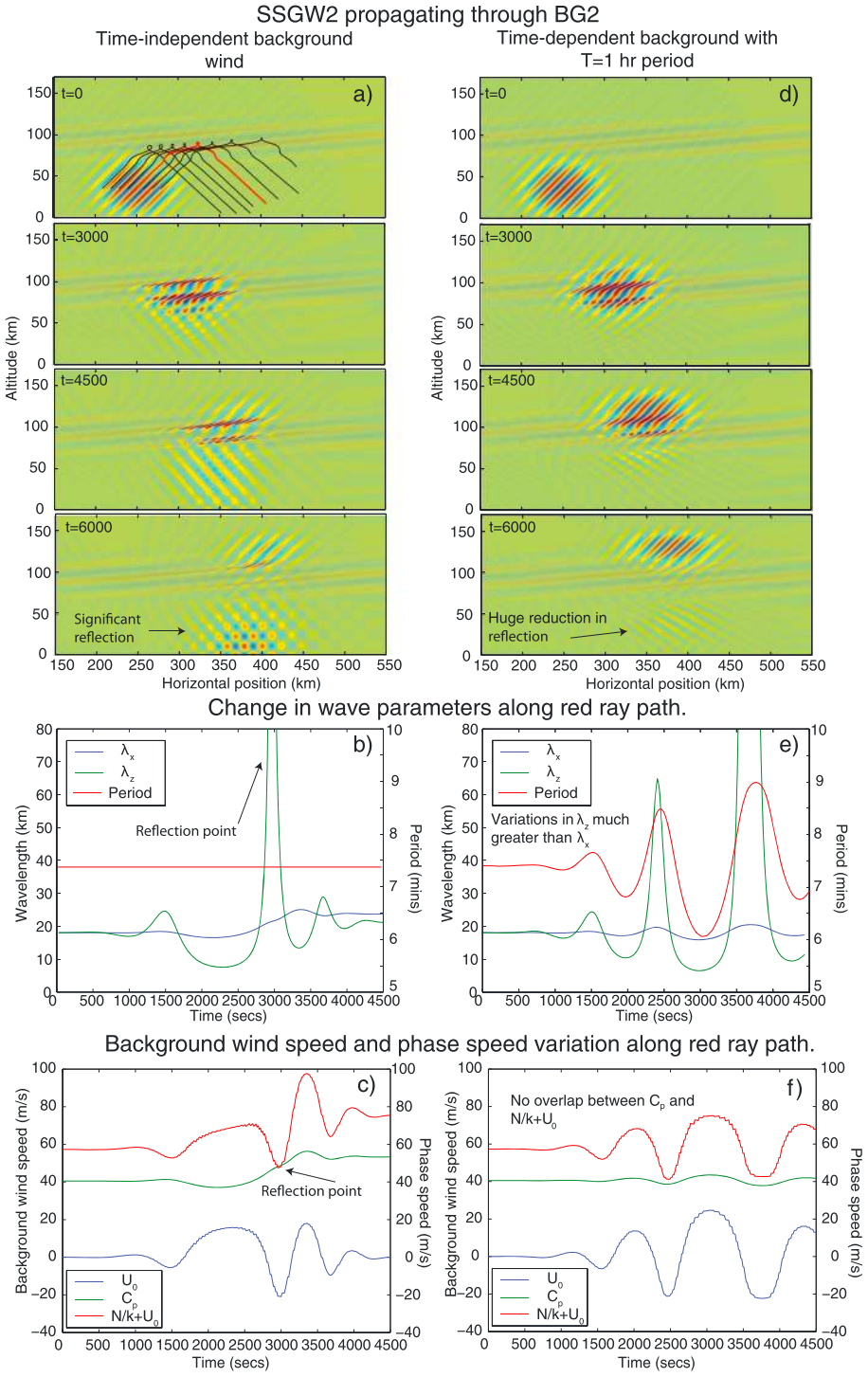

Figure 7. The propagation of SSGW2 through BG2 at four different times for (a) the time-independent background case and (d) adding a time-dependent phase progression of the background wave. The black lines represent the ray trace paths, and the remaining figures show the changes in (b,e) wave parameters and (c,f) background wind, reflection condition ($N/k + U_0$), and small-scale wave phase speed along the raypath.

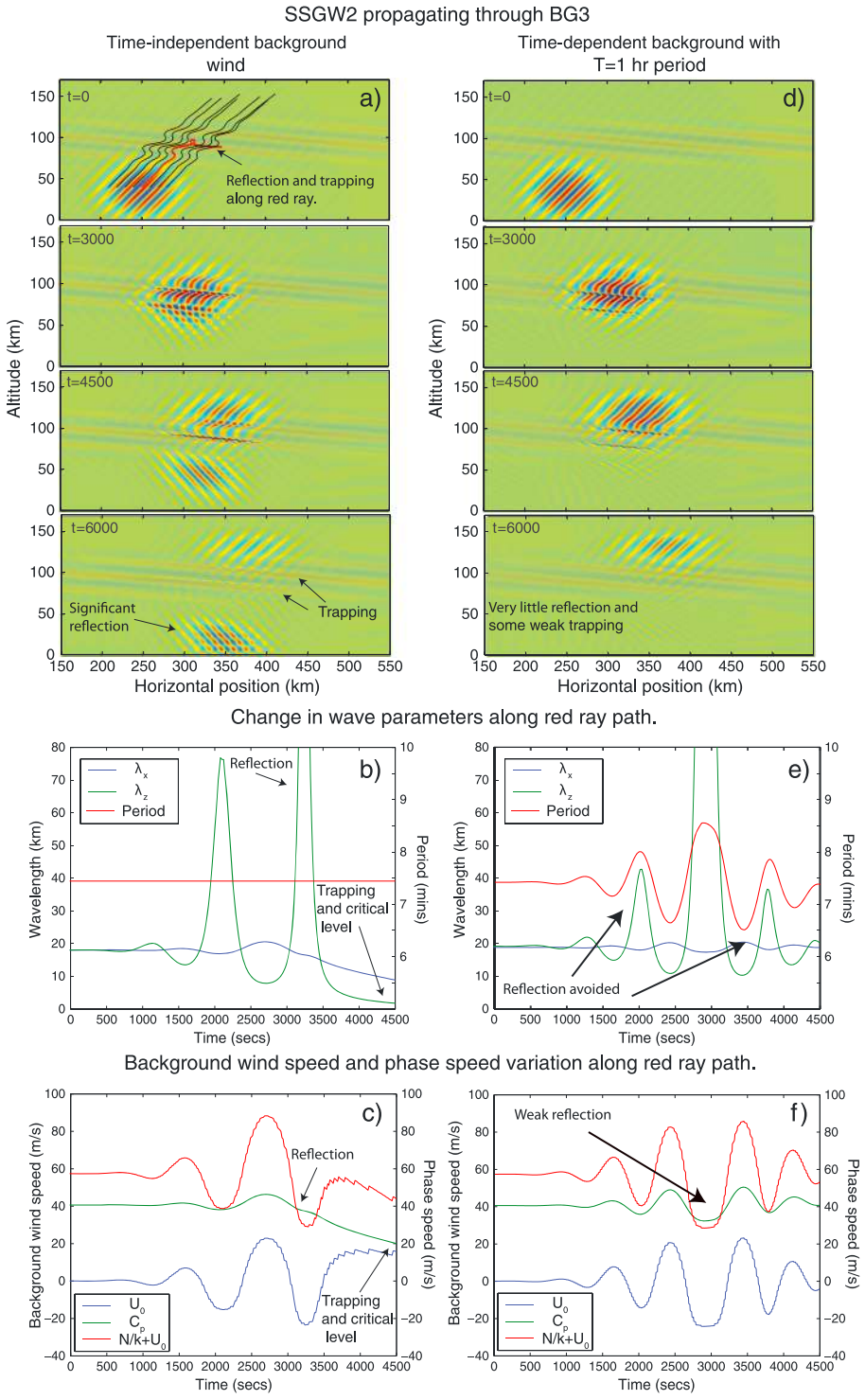

Figure 8. The propagation of SSGW2 through BG3 at four different times for (a) the time-independent background case and (d) adding a time-dependent phase progression of the background wave. The black lines represent the ray trace paths, and the remaining figures show the changes in (b,e) wave parameters and (c,f) background wind, reflection condition ($N/k + U_0$), and small-scale wave phase speed along the raypath.

Figure 5d shows the case where the background wave wind field has an associated phase progression (Period = 1 h) in the same direction as that of the small-scale wave. The effect of the inclusion of the background wind phase progression is to reduce the amount of critical-level filtering and increase transmission. This effect has been noted before in *z-t* ray tracing domains [e.g., *Eckermann*, 1997; *Walterscheid*, 2000; *Sartelet*, 2003; *Vanderhoff et al.*, 2008; *Senf and Achatz*, 2011]. This is suggested to occur due to two factors: (1) The critical level evolves with the phase of the background wave, thus the interaction time between the small-scale wave and the critical level is reduced and more of the small-scale wave amplitude is retained. (2) The time dependence of the background wind induces a change in period of the small-scale wave [e.g., *Huang et al.*, 2013], which acts to reduce critical-level effects. This effect is illustrated in Figure 5e, which shows the period of the small-scale wave varying in time along with the wavelengths. Figure 5f supports these conclusions further by showing that the horizontal phase speed of the small-scale wave oscillates with the background wind velocity (as a result of the changing period), but the two no longer cross as they did for the static case and the critical-level condition is no longer met. Crucially, this reduction of critical-level filtering means that parameterization schemes, which can neglect time-dependent effects, tend to overestimate obliteration of waves by filtering effects [e.g., *Eckermann*, 1997; *Vanderhoff et al.*, 2008; *Senf and Achatz*, 2011].

In Figure 6, the phase fronts of the background wave wind field (BG3) are defined by a negative K value (left going when phase progression is included). For the time-dependent case this means that the horizontal phase velocities of the background and small-scale wave are opposite. We do not see any strong evidence of critical-level filtering in either the time-dependent or time-independent cases. There is some evidence of weak reflection in the time-independent case but virtually nothing in the time-dependent case. The vertical and horizontal wavelengths oscillate in antiphase with each other due to the differing orientation of the background wave relative to the small-scale wave. When the horizontal wave number of both waves have the same sign such as in the BG2 simulations, the small-scale wave tends to be channeled along the phase fronts of the background wave where it undergoes critical-level filtering. However, when the wave numbers have opposite sign (i.e., the BG3 case), the refraction acts to avoid the trapping of the small-scale wave along the phase fronts of the background wave unless the small-scale wave is first reflected downward (which changes the sign of m, and thus the orientation of the phase fronts relative to the background wind).

In the time-dependent case, the horizontal phase velocity of the background wave and the group velocity of the small-scale packet oppose each other, thus, in the frame of the small-scale wave, the phase fronts of the background wave approach the SSGW more rapidly than for BG2 in Figure 5. This, combined with the lack of small-scale wave trapping along the medium-scale wave phase fronts, means that there is virtually no filtering at all. Due to the rapid change in background wind along a raypath, the period of the small-scale wave also varies relatively rapidly. Crucially, it varies in phase with the vertical wavelength, so when the vertical wavelength increases and tends toward a reflection-type scenario, the period also increases, reducing the tendency for reflection. It can also be seen in Figure 6f that the horizontal phase speed of the small-scale wave changes more rapidly and by a larger amount than the static case, thus reducing the amount of time the wave would interact at either a critical or reflection level.

It is clear from these simulations that the inclusion of background time dependence and the relative direction of propagation of the two waves are important factors to consider in the propagation of small-scale waves through medium-scale wave fields.

4.2. Propagation of SSGW2

When specifying a small-scale gravity wave using the SSGW2 parameters, the vertical group velocity is approximately double that of SSGW1. This means that the packet is more prone to reflection, but it also means that vertical variations in the background wind become more important than horizontal variations. The reflection condition for gravity waves is when $\Omega = N$, or $C_p = N/k + U_0$. Therefore, we add the plot of $N/k + U_0$ to Figures 7c, 7f, 8c, and 8f.

Figure 7a (BG2) shows that a significant portion of the packet is reflected in the static case. The reflection occurs predominately along the largest magnitude negative phase front of the background wind. Because this phase front is slanted, different parts of the small-scale packet are reflected at different altitudes. While the ray trace suggests that the small-scale wave is completely reflected, in reality some portion of the wave is transmitted as shown by the simulation results. The reflection point along the red raypath is indicated by the large increase in vertical wavelength in Figure 7b and the point where C_p crosses $N/k + U_0$ in Figure 7c.

For the time-dependent background wave (Figure 7d), the amount of wave energy reflected is significantly reduced, just as it was for SSGW1 with critical-layer filtering. Therefore, inclusion of time dependence of a background wind field can reduce both critical-level and reflection-based filtering. Note that the variations in the horizontal wavelength and period are much smaller in magnitude than they were for SSGW1 due to the larger vertical group velocity of SSGW2. Therefore, the relative interaction time between the small-scale and medium-scale waves, as well as the horizontal variation the small-scale wave experiences, is reduced. However, the variation in period of the small-scale wave is sufficient to avoid C_p crossing $N/k + U_0$ (Figure 7f) and thus avoiding significant reflection.

Figure 8a (BG3) shows an interesting case where reflection occurs, followed by wave trapping and critical-level filtering. This is exactly what happens along the red raypath. As mentioned previously, trapping and channeling of the small-scale wave tend to occur when the small- and medium-scale waves both have similar phase front orientations. However, when they are opposing, trapping is suppressed. In this case, reflection of the small-scale wave changes the orientation of the phase fronts (since $-m$ becomes $+m$) so that the orientation of the small- and medium-scale waves become similar, and the small-scale wave becomes trapped. While some portion of the wave energy is reflected and then trapped, the majority is reflected without trapping, leaving only a relatively small amount of energy that is transmitted into the thermosphere without reflection. This differs from the ray trace paths which suggests that the majority of the small-scale wave packet should be transmitted. The reflection and trapping of the wave is clearly indicated in Figures 8b and 8c. We see that the vertical wavelength approaches infinity and C_p crosses $N/k + U_0$ as the small-scale wave reflects, and then the vertical wavelength tends toward zero and C_p approaches U_0 as the small-scale wave becomes trapped and undergoes critical-level filtering.

For the time-dependent background case, we see a significant reduction in reflection and subsequent wave trapping. The vertical wavelength variations are significantly reduced as a result of the changes in period of the small-scale wave. It is worth noting that, while the vertical wavelength does become very large near 3000s in the ray tracing, the reflections that do occur are appear relatively weak in the 2D model, with significant vertical tunneling. This is especially apparent when compared with the time-independent background, where a significant reflection event occurs through the same wave field.

4.3. Kinetic Energy Density Evolution

In order to better assess wave energy evolutions during the simulations, we plot the perturbation kinetic energy density, summed over the whole domain and normalized to the initial value, for each of the different scenarios simulated in Figures 9a and 9b. We also estimate the relative amount of energy which is transmitted in comparison to that reflected for the SSGW2 simulations. This is done by summing the normalized kinetic energy density below and above 95 km individually. The kinetic energy density that makes it above 95 km (where the background wave is centered and at maximum amplitude) is considered as transmitted, while that below 95 km is considered as reflected. The results of this are shown in Figures 9c and 9d.

From Figure 9a, when considering the SSGW1 simulations, it is clear that there is a much greater loss (by 7500 s) when the background wave wind field is static (especially for BG2). For the case of BG2 (when the small-scale and background waves have the same direction of horizontal phase progression), the reduction in kinetic energy loss by including background time dependence is ~60%, whereas for BG3 (when the small-scale and background waves have opposing horizontal phase progression), the time-independent case retains about 10% more kinetic energy than the time-dependent case. However, propagation through a static background with opposing phase progressions still retains ~3% more energy than a time-dependent background whose phase progression is in the same direction as the small-scale wave.

For the propagation of the reflection prone SSGW2 (Figure 9b), it is the static background simulations which retain the most energy density after 7500 s. This is because the lack of wave reflection and increased transmission in the time-dependent cases lead to more dissipation of wave energy in the thermosphere, and thus a more rapid decline in energy overall. This is illustrated better in Figures 9c and 9d, where the kinetic energy is split into that which is above and below 95 km altitude. For the time-dependent simulations, ~80–90% of the initial kinetic energy is transmitted up into the thermosphere and is dissipated, whereas the fraction is only ~30–50% for the static background wind wave field. For parameterizations that do not include background

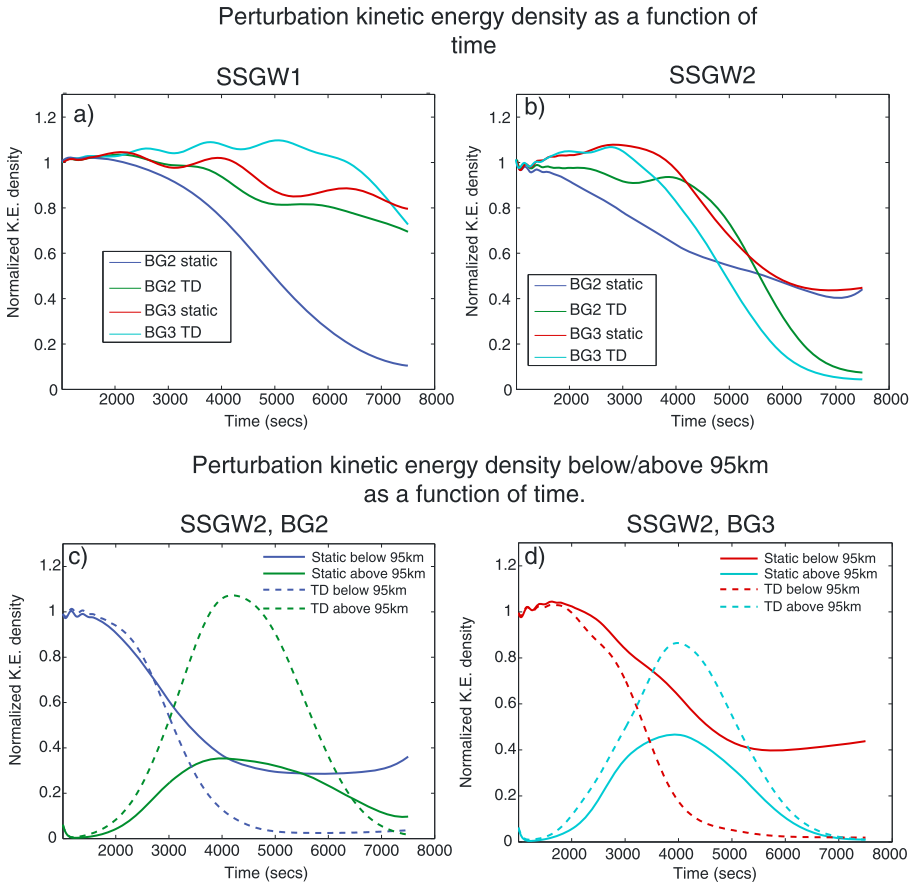

Figure 9. The kinetic energy density, normalized to the initial value and summed over (a, b) the entire domain and (c, d) the region of the domain below and above 95 km individually. In each case the label "static" refers to the nonevolving background case, while "TD" refers to the time-dependent background case.

time dependence (but do include reflection), the model could underestimate the wave forcing in the thermosphere. Furthermore, parameterizations neglect reflection and transmission of high-frequency gravity waves, which nevertheless carry significant momentum [*Fritts and Alexander*, 2003].

4.4. Propagation Through a Nonisothermal Background

We include, for comparison, the propagation of SSGW2 through BG2 with an arbitrary realistic background atmosphere specified using NRLMSISE-00 [*Picone et al.*, 2002] (see Figure 10). In this case both the varying buoyancy frequency and the background wind act to refract and reflect the SSGW. Instead of using initial conditions to specify SSGW2, we now excite it using a time-dependent body forcing so the wave will conform to the dispersion parameters of the background atmosphere profile. This also means that the wave excited has both upward and downward propagating components. Note that for simplification, the thermal structure of the BG2 medium-scale wave and its refraction by the background temperature structure are omitted. These effects will be considered in further studies.

The inclusion of the realistic background atmosphere makes two key differences in these simulations as can be seen in Figure 11. First, the thermospheric temperature acts to dramatically increase the vertical wavelength of SSGW2. This makes the packet far more susceptible to the effects of reflection, thus we see a dramatic reduction in amplitude above ~120 km as the wave energy is partially reflected here. Second, the thermal structure of the stratosphere has a tendency to trap short-period gravity waves [*Heale et al.*, 2014a]; therefore, a portion of the packets' energy and momentum remains in this region of the atmosphere and undergoes reflection at the tropopause. The time-dependent case still facilitates more upward propagating than the time-independent case, although SSGW2 is rapidly attenuated in the lower thermosphere in both cases.

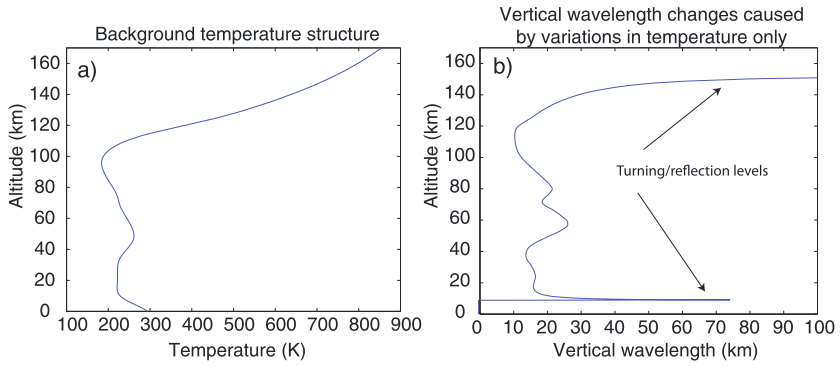

Figure 10. (a) NRLMSIS-00 specified background temperature and (b) the vertical wavelength change with altitude due to the varying buoyancy frequency.

The perturbation horizontal wind tends to be maximized along the background wind lines of the maximum positive phase, and there is reduced reflection from the medium-scale wave.

Figure 12 shows the domain-averaged kinetic energy density above and below 95 km, as described in section 4.3. Due to the time-dependent nature of the wave forcing in the nonisothermal simulations, the kinetic energy increases from the first 3000 s as the wave is excited. All values are normalized to the peak kinetic energy. Comparison of the static and time-dependent cases shows, much as before, that the time-dependent simulation facilitates a greater amount of wave energy into the thermosphere. At 5500 s, there is ~15% more kinetic energy transmitted into the thermosphere for the time-dependent case. The second peak in the green line is due to the initial downward propagating wave, which reflects off the tropopause and reaches 95 km altitude at late times. The propagation—and also interaction—of waves through nonisothermal backgrounds will be studied in more detail in further studies.

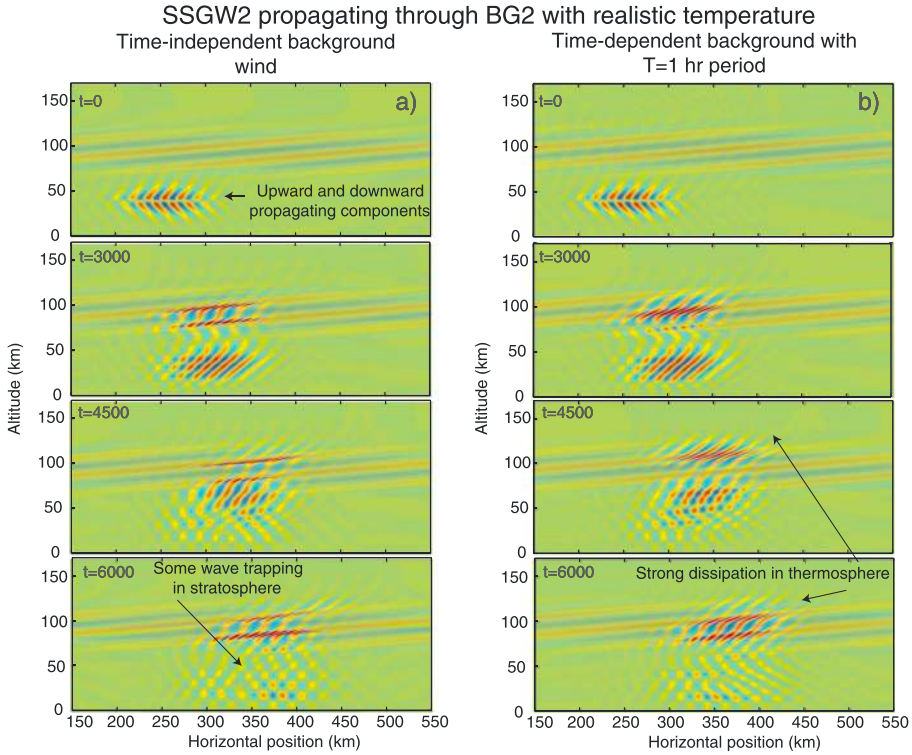

Figure 11. The propagation of SSGW2 through BG2, with a realistic background atmosphere at four different times for (a) the time-independent background case and (b) adding a time-dependent phase progression of the background wave.

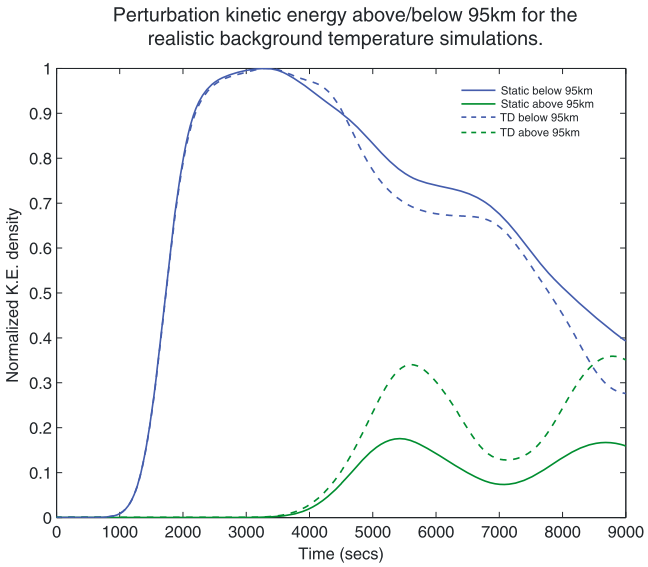

Figure 12. The kinetic energy density, normalized to the peak value and summed over the region of the domain below and above 95 km individually. In each case the label "static" refers to the nonevolving background case, while "TD" refers to the time-dependent background case. These are for the nonisothermal simulations.

5. Summary and Conclusions

In this paper, we used a combination of 2-D compressible simulations and ray tracing techniques to simulate the linear propagation of two gravity wave packets (one prone to critical-level filtering, the other more prone to reflection) through horizontally and vertically inhomogeneous background winds. This included a purely vertically and horizontally varying horizontal wind and two medium-scale background wind wave fields, whose horizontal phase propagated with and against that of the small-scale wave. Our 2-D compressible model leverages a new method for incorporating inhomogeneity for weakly nonlinear problems, which may be of significant utility for future studies.

The purely vertically varying horizontal background wind provides the familiar reflection and critical-level scenarios, with a varying vertical wavelength and constant horizontal wavelength. We find that for a purely horizontally varying horizontal background wind, the horizontal wavelength of the small-scale wave decreases or increases depending on whether the background wind speed is decreasing or increasing in the horizontal, while the vertical wavelength remains constant. We find a decent agreement between the model and basic inviscid dispersion relation [*Nappo*, 2002]; however, the theoretical result predicts a larger change in wavelength than those derived from the model, due most likely to finite resolution.

We also observe the presence of a horizontal "blocking point" as described in *Basovich and Tsimring* [1984], which occurs when the wave propagation direction and background wind velocities are in opposite directions. If the background wind is strong enough, the horizontal group velocity approaches zero and the horizontal wavelength of the packet shrinks indefinitely. There is good agreement between the theoretical and modeled wind speed needed to induce a blocking point, with values of −8.57 and −8.5 m/s, respectively, for the packet simulated.

When a small-scale wave interacts with a static medium-scale wave of sufficiently large amplitude, it can be channeled along the phase fronts of the background wave and undergo critical-level filtering or it can be strongly reflected, depending on the parameters of the waves. It is also possible that an upward propagating gravity wave will be reflected by the background wave and then channeled along its phase fronts and subsequently critical-level filtered. When time-dependent phase progression is added to the background wave, the effects of critical-level filtering and reflection are significantly reduced (as much as 70% in our simulations). The reduction in filtering caused by the inclusion of time dependence is likely the result of the following: (1) The phase progression of the background wave means that a small-scale wave has less interaction time with a perceived critical or reflection level. (2) The time-dependence of the background wave induces a change in ground-relative frequency of the small-scale wave, which acts to avoid critical levels or reflection.

The direction of the propagation of the small-scale wave with respect to the phase progression of the background wind also made a considerable difference to the filtering. When the small-scale wave propagates in the same horizontal direction as the background wave horizontal phase progression, then the small-scale wave is far more likely to experience trapping, channeling, and critical-level filtering than if the directions are opposite. This happens regardless of whether time dependence of the background wave is included. This occurs due to the way the background wind acts to refract the small-scale wave. When the phases are progressing in the same direction, the horizontal and vertical wavelengths will both increase and decrease together in phase, directing the small-scale waves in between the background phase fronts. When the phase progression directions are different, the vertical wavelength will increase while the horizontal wavelength will decrease and vice versa. Therefore, the small-scale wave tends to be accelerated, reducing trapping.

As the vertical group velocity of the small-scale packet increases, the wave becomes more prone to reflection but the horizontal and temporal variations in the background wave wind field matter less. Subsequently, the magnitude of the changes in horizontal wavelength and the period of the small-scale wave are smaller.

The inclusion of background wave time dependence and consideration of its propagation relative to a small-scale packet are important factors in parameterization schemes and filtering of small-scale waves. Propagation of small-scale waves against the time-dependent phase progression direction of the background wave will likely reduce the critical-level and reflection effects the most. This is because the change in the background wind along the raypaths of the small-scale wind are greatest in this scenario, thus the ground relative frequency of the small-scale wave changes the most rapidly avoiding critical-level or reflection conditions. These effects on critical levels are consistent with past findings [e.g., *Eckermann*, 1997; *Vanderhoff et al.*, 2008; *Senf and Achatz*, 2011], and results also reinforce the important role of medium-scale dynamics for reflection and ducting, especially for short-period waves that may carry significant momentum. The additional impacts of medium scale variations in thermal structure will be investigated in future studies.

Acknowledgments
Research by C. J. Heale and J. B. Snively was supported under NSF grants AGS-1151746 and AGS-1344356. Copies of the simulation data and figures can be obtained on request to the authors at healec@erau.edu.

References

Badulin, S. I., and V. I. Shriria (1993), On the irreversibility of internal-wave dynamics due to wave trapping by mean flow inhomogeneities. Part 1. Local analysis, *J. Fluid Mech.*, *251*, 21–53.

Badulin, S. I., V. I. Shriria, and L. S. Tsimring (1985), The trapping and vertical focusing of internal waves in a pycnocline due to horizontal inhomogeneities of density and currents, *J. Fluid Mech.*, *158*, 199–218.

Bakas, N. A., and B. F. Farrell (2008), Gravity waves in a horizontal shear flow. Part I: Growth mechanisms in the absence of potential vorticity perturbations, *J. Phys. Oceanogr.*, *39*, 481–496, doi:10.1175/2008JPO3836.1.

Bale, D. S., R. J. LeVeque, S. Mitran, and J. A. Rossmanith (2002), A wave propagation method for conservation laws and balance laws with spatially varying flux functions, *J. Sci. Comput.*, *24*(3), 955–978.

Banks, P. M., and G. Kockarts (1973), *Aeronomy*, Academic Press, New York.

Basovich, A. Y., and L. S. Tsimring (1984), Internal waves in a horizontally inhomogeneous flow, *J. Fluid Mech.*, *142*, 233–249.

Blumen, W. (1985), Reflection of hydrostatic gravity waves in a stratified shear flow. Part I: Theory, *J. Atmos. Sci.*, *42*, 2255–2263.

Booker, J. R., and F. P. Bretherton (1967), The critical layer for internal gravity waves in a shear flow, *J. Fluid Mech.*, *27*, 513–539.

Bretherton, F. P. (1966), The propagation of groups of internal waves in a shear flow, *Q. J. R. Meteorol. Soc.*, *92*, 466–480.

Broutman, D., and W. Young (1986), On the interaction of small-scale oceanic internal waves with near-inertial waves, *J. Fluid Mech.*, *166*, 341–358.

Chimonas, G., and C. O. Hines (1986), Doppler ducting of atmospheric gravity waves, *J. Geophys. Res.*, *91*(D1), 1219–1230.

Djuth, F. T., M. P. Sulzer, S. A. Gonzeles, J. D. Mathews, J. H. Elder, and R. L. Walterscheid (2004), A continuum of gravity waves in the Arecibo thermosphere, *Geophys. Res. Lett.*, *31*, L16801, doi:10.1029/2003GL019376.

Dunkerton, T. J. (1981), Wave transience in a compressible atmosphere. Part I: Transient internal wave, mean flow interaction, *J. Atmos. Sci.*, *38*, 281–297.

Dunkerton, T. J., and D. C. Fritts (1984), Transient gravity-wave critical layer interaction. Part I: Convective adjustment and the mean zonal acceleration, *J. Atmos. Sci.*, *41*, 992–1007.

Eckermann, S. D. (1997), Influence of wave propagation on the Doppler spreading of atmospheric gravity waves, *J. Atmos. Sci.*, *54*, 2554–2573.

Einaudi, F., and C. O. Hines (1971), WKB approximation in application to acoustic-gravity waves, *Can. J. Phys.*, *48*, 1458–1471.

Fritts, D., and M. J. Alexander (2003), Gravity wave dynamics and effects in the middle atmosphere, *Rev. Geophys.*, *41*(1), 1003, doi:10.1029/2001RG000106.

Fritts, D. C. (1984), Gravity wave saturation in the middle atmosphere: A review of theory and observations, *Rev. Geophys.*, *22*, 275–308.

Fritts, D. C., and T. J. Dunkerton (1985), Fluxes of heat and constituents due to convectively unstable gravity waves, *Ann. Geophys.*, *68*, 247–265.

Fritts, D. C., and T. S. Lund (2011), Gravity wave influences in the thermosphere and ionosphere: Observations and recent modeling, in *Aeronomy of the Earth's Atmosphere and Ionosphere*, vol. 2, edited by M. Abdu and D. Pancheva, pp. 109–130, Springer, Netherlands.

Fritts, D. C., and R. Vincent (1987), Mesospheric momentum flux studies at Adelaide, Australia, *J. Atmos. Sci.*, *44*, 605–619.

Fritts, D. C., and L. Yuan (1989), An analysis of gravity wave ducting in the atmosphere: Eckart's resonances in thermal and Doppler ducts, *J. Geophys. Res.*, *94*(D15), 18,455–18,466.

Fritts, D. C., J. F. Garten, and O. Andreasson (1996), Wave breaking and transition to turbulence in stratified shear flows, *J. Atmos. Sci.*, *53*, 1057–1085.

Fritts, D. C., S. L. Vadas, K. Wan, and J. A. Werne (2006), Mean and variable forcing of the middle atmosphere by gravity waves, *J. Atmos. Sol. Terr. Phys.*, *68*, 247–265.
Hartman, R. J. (1975), Wave propagation in a stratified shear flow, *J. Fluid Mech.*, *71*, 89–104.
Heale, C. J., J. B. Snively, and M. P. Hickey (2014a), Numerical simulation of the long-range propagation of gravity wave packets at high latitudes, *J. Geophys. Res. Atmos.*, *119*, 11,116–11,134, doi:10.1002/2014JD022099.
Heale, C. J., J. B. Snively, M. P. Hickey, and C. J. Ali (2014b), Thermospheric dissipation of upward propagating gravity wave packets, *J. Geophys. Res. Space Physics*, *119*, 3857–3872, doi:10.1002/2013JA019387.
Hecht, J., R. L. Walterscheid, M. P. Hickey, and S. Franke (2001), Climatology and modeling of quasi-monochromatic atmospheric gravity waves observed over Urbana, Illinois, *J. Geophys. Res.*, *106*(D6), 5181–5195.
Hocke, K., and T. Tsuda (2001), Gravity waves and ionospheric irregularities over tropical convection zones observed by GPS/MET radio occultation, *Geophys. Res. Lett.*, *28*, 2815–2818.
Holton, J. R. (1982), The role of gravity wave induced drag and diffusion in the momentum budget of the mesosphere, *J. Atmos. Sci.*, *39*, 791–799.
Holton, J. R. (1983), The influence of gravity wave breaking on the general circulation of the middle atmosphere, *J. Atmos. Sci.*, *40*, 2497–2507.
Huang, C. M., S. D. Zhang, F. Yi, K. M. Huang, Y. H. Zhang, Q. Gan, and Y. Gong (2013), Frequency variations of gravity waves interacting with a time-varying tide, *Ann. Geophys.*, *31*, 1731–1743, doi:10.5194/angeo-31-1731-2013.
Huang, K. M., S. D. Zhang, and F. Yi (2008), Propagation and reflection of gravity waves in a meridionally sheared wind field, *J. Geophys. Res.*, *113*, D09106, doi:10.1029/2007JD008877.
Hung, R. J., and J. P. Kuo (1978), Ionospheric observations of gravity-waves associated with hurricane Eloise, *J. Geophys. Res.*, *45*, 67–80.
Isler, J., M. Taylor, and D. Fritts (1997), Observational evidence of wave ducting and evanescence in the mesopshere, *J. Geophys. Res.*, *102*, 26,301–26,312.
Kelley, M. C. (1997), In situ ionospheric observations of severe weather-related gravity waves and associated small-scale plasma structure, *J. Geophys. Res.*, *102*, 329–336.
LeVeque, R. J., and M. J. Berger (2004), Clawpack software version 4.6. [Available at www.clawpack.org.]
Lighthill, J. (1978), *Waves in Fluids*, Cambridge Univ. Press, Cambridge.
Lindzen, R. S. (1981), Turbulence and stress owing gravity wave and tidal breakdown, *J. Geophys. Res.*, *86*(C10), 9707–9714.
Liu, X., J. Xu, J. Yue, and S. L. Vadas (2013), Numerical modeling study of the momentum deposition of small amplitude gravity waves in the thermosphere, *Ann. Geophys.*, *31*, 1–14.
Nappo, C. J. (2002), *An Introduction to Atmospheric Gravity Waves*, Academic, San Diego, Calif.
Olbers, D. J. (1981), The propagation of internal waves in a geostrophic current, *J. Phys. Oceanogr.*, *11*, 1224–1233.
Oliver, W., Y. Otsuka, M. Sato, T. Takami, and S. Fukao (1997), A climatology of F region gravity wave propagation over the middle and upper atmosphere radar, *J. Geophys. Res.*, *102*, 14,499–14,512.
Picone, J. M., A. E. Hedin, D. P. Drob, and A. Aikin (2002), NRL-MSISE-00 empirical model of the atmosphere: Statisical comparisons and scientific issues, *J. Geophys. Res.*, *107*(A12), 1468, doi:10.1029/2002JA009430.
Pitteway, M. L. V., and C. O. Hines (1963), The viscous damping of atmospheric gravity waves, *Can. J. Phys.*, *41*, 1935–1948.
Robinson, T. R. (1997), Nonlinear reflection of internal gravity waves by thermospheric winds, *Adv. Space Res.*, *20*, 1261–1264.
Roe, P. L. (1981), Approximate Riemann solvers, parameter vectors and difference schemes, *J. Comput. Sci.*, *43*, 357–372.
Sartelet, K. N. (2003), Wave propagation inside an inertial wave. Part I: Role of time dependence and scale separation, *J. Atmos. Sci.*, *60*, 1433–1447.
Senf, F., and U. Achatz (2011), On the impact of middle-atmosphere thermal tides on the propagation and dissipation of gravity waves, *J. Geophys. Res.*, *116*, D24110, doi:10.1029/2011JD015794.
Snively, J. B. (2013), Mesospheric hydroxyl airglow signatures of acoustic and gravity waves generated by transient tropospheric forcing, *Geophys. Res. Lett.*, *40*, 4533–4537, doi:10.1002/grl.50886.
Snively, J. B., and V. P. Pasko (2008), Excitation of ducted gravity waves in the lower thermosphere by tropospheric sources, *J. Geophys. Res.*, *113*, A06303, doi:10.1029/2007JA012693.
Snively, J. B., V. Pasko, M. J. Taylor, and W. K. Hocking (2007), Doppler ducting of short-period gravity waves by midlatitude tidal wind structure, *J. Geophys. Res.*, *112*, A03304, doi:10.1029/2006JA011895.
Sutherland, B. R. (1999), Propagation and reflection of internal waves, *Phys. Fluids*, *11*, 1081–1090.
Sutherland, B. R. (2000), Internal wave reflection in uniform shear, *Q. J. R. Meteorol. Soc.*, *126*, 3255–3287.
Suzuki, S., K. Shiokawa, Y. Otsuka, S. Karwamura, and Y. Murayama (2013a), Evidence of gravity wave ducting in the mesopause region from airglow network observations, *Geophys. Res. Lett.*, *40*, 601–605, doi:10.1029/2012GL054605.
Suzuki, S., S. L. Vadas, K. Shiokawa, Y. Otsuka, S. Karwamura, and Y. Murayama (2013b), Typoon-induced concentric airglow structures in the mesopause region, *Geophys. Res. Lett.*, *40*, 5983–5987, doi:10.1002/2013GL058087.
Taylor, M. J., D. N. Turbull, and R. P. Lowe (1995), Spectrometric and imaging measurements of a spectacular gravity wave event observed during the ALOHA-93 campaign, *Geophys. Res. Lett.*, *22*(20), 2848–2852.
Taylor, M. J., P. D. Pautet, A. F. Medeiros, R. Buriti, J. Fechine, D. C. Fritts, S. L. Vadas, H. Takahashi, and F. T. Sao Sabbas (2009), Characteristics of mesospheric gravity waves near the magnetic equator, Brazil, during the SpreadFEx campaign, *Ann. Geophys.*, *27*, 461–472, doi:10.5194/angeo-27-461-2009.
Thorpe, S. A. (1981), An experimental study of critical layer, *J. Fluid Mech.*, *103*, 321–344.
Torrence, C., and G. P. Compo (1998), A practical guide to wavelet analysis, *Bull. Am. Meteorol. Soc.*, *79*, 61–78.
Vadas, S. L. (2007), Horizontal and vertical propagation and dissipation of gravity waves in the thermosphere from lower atmospheric and thermospheric sources, *J. Geophys. Res.*, *112*, A06305, doi:10.1029/2006JA011845.
Vadas, S. L., and D. C. Fritts (2006), Influence of solar variability on gravity wave structure and dissipation in the thermosphere from tropospheric convection, *J. Geophys. Res.*, *111*, A10S12, doi:10.1029/2005JA011510.
Vadas, S. L., and H. L. Liu (2009), Generation of large-scale gravity waves and neutral winds in the thermosphere from the dissipation of convectively generated gravity waves, *J. Geophys. Res.*, *114*, A10310, doi:10.1029/2009JA014108.
Vanderhoff, J. C., K. K. Nomura, J. W. Rottman, and C. Macaskill (2008), Doppler spreading of internal gravity waves by an inertia-wave packet, *J. Geophys. Res.*, *113*, C05018, doi:10.1029/2007JC004390.
Vincent, R. A., and I. M. Reid (1983), HF Doppler measurements of mesospheric momentum fluxes, *J. Atmos. Sci.*, *40*, 1321–1333.
Walterscheid, R., J. Hecht, R. Vincent, I. Reid, J. Woithe, and M. P. Hickey (1999), Analysis and interpretation of airglow and radar observations of quasi-monochromatic gravity waves in the upper mesosphere and lower thermosphere over Adelaide, Australia, *J. Atmos. Sol. Terr. Phys.*, *61*(6), 461–478.

Walterscheid, R., G. Schubert, and D. Brinkman (2001), Small-scale gravity waves in the upper mesosphere and lower thermosphere generated by deep tropical convection, *J. Geophys. Res.*, *106*(D23), 31,825–31,832.

Walterscheid, R. L. (2000), Propagation of small-scale gravity waves through large-scale internal wave field: Eikonal effects at low-frequency approximation critical levels, *J. Geophys. Res.*, *105*(D14), 18,027–18,037.

Walterscheid, R. L., and M. P. Hickey (2011), Group velocity and energy flux in the thermosphere: Limits on the validity of group velocity in a viscous atmosphere, *J. Geophys. Res.*, *116*, D12101, doi:10.1029/2010JD014987.

Wang, D. Y., and T. F. Tuan (1988), Brunt-Doppler ducting of small period gravity waves, *J. Geophys. Res.*, *93*(A9), 9916–9926.

Yiğit, E., A. D. Aylward, and A. S. Medvedev (2008), Parameterization of the effects of vertically propagating gravity waves for thermosphere general circulation models: Sensitivity study, *J. Geophys. Res.*, *113*, D19106, doi:10.1029/2008JD010135.

Yiğit, E., A. S. Medvedev, A. D. Aylward, P. Hartogh, and M. J. Harris (2009), Modeling the effects of gravity wave momentum deposition on the general circulation above the turbopause, *J. Geophys. Res.*, *114*, D07101, doi:10.1029/2008JD011132.

Yu, Y., and M. P. Hickey (2007), Time-resolved ducting of atmospheric acoustic-gravity waves by analysis of the vertical energy flux, *Geophys. Res. Lett.*, *34*, L02821, doi:10.1029/2006GL028299.

Yu, Y., M. Hickey, and Y. Liu (2009), A numerical model characterizing internal gravity wave propagation into the upper atmosphere, *Adv. Space Res.*, *44*(7), 836–846.

Zhang, S. D., and F. Yi (2002), A numerical study of propagation characteristics of gravity wave packets propagating in a dissipative atmosphere, *J. Geophys. Res.*, *D14*, 4222, doi:10.1029/2001JD000864.